ACS OMEGA

http://pubs.acs.org/journal/acsodf

Article

Flexible and Freestanding MoS_2 Nanosheet/Carbon Nanotube/Cellulose Nanofibril Hybrid Aerogel Film for High-Performance All-Solid-State Supercapacitors

Huanjun Chang, Longfei Zhang, Shaoyi Lyu,* and Siqun Wang

Cite This: *ACS Omega* 2022, 7, 14390−14399

Read Online

ACCESS | Metrics & More | Article Recommendations | Supporting Information

ABSTRACT: Flexible supercapacitors assembled with two-dimensional materials have become a research hotspot in recent years. Here, we have prepared two-dimensional nanomaterial MoS_2 and SWCNT, CNF aerogel composite electrode, and its flexible all-solid-state supercapacitor. SWCNT can inhibit the accumulation of MoS_2 nanosheets and enhance the conductivity of the composite electrode. CNF can improve the dispersion uniformity of MoS_2 and SWCNT, and endow the composite electrode with a high specific surface area (328.86 m^2 g^{-1}) and excellent flexibility. MoS_2−SWCNT/CNF supercapacitor has a good rectangular CV curve and symmetrical triangular GCD curve. The CV curve of the MoSCF3 supercapacitor with the highest MoS_2−SWCNT content remains rectangular even at the scanning rate of 2000 mV s^{-1}. Its voltage window can reach 1.5 V. MoS_2−SWCNT/CNF supercapacitor has a specific capacity of 605.32 mF cm^{-2} (scanning rate of 2 mV s^{-1}) and 30.34 F g^{-1} (0.01 A g^{-1}), an area specific energy of 35.61 mWh cm^{-2} (area specific power of 0.03 mW cm^{-2}), and extremely high cycle stability (91.01% specific capacity retention rate after 10 000 cycles) and good flexibility. The fine nanocomposite structure gives MoS_2−SWCNT/CNF supercapacitor impressive electrochemical performance and excellent flexibility, which can be used in the field of portable electronic devices and flexible devices.

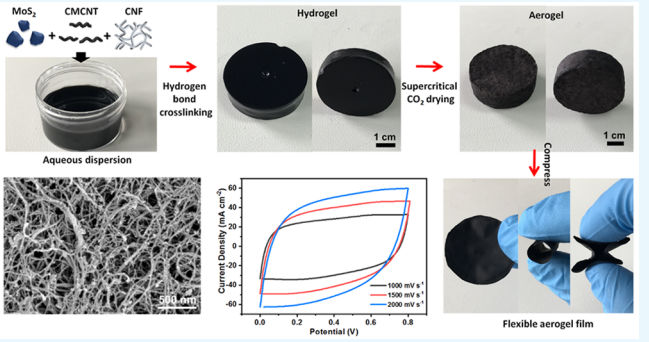

INTRODUCTION

Flexibility, compactness, and agility have become the main development direction of portable electronic devices and wearable devices.[1,2] Exploring and developing new flexible energy storage devices that are miniaturized, lightweight, high energy density, long cycle life, and able to withstand certain deformation are urgent requirements for the development of portable intelligent electronic devices and flexible display screens.[3−5] Supercapacitor has attracted extensive attention because of its advantages of fast charge and discharge speed and high power density. It has made many new achievements in electrode material preparation, device design, and assembly. Among them, the flexible all-solid-state supercapacitor based on polymer gel electrolyte has the characteristics of a simple assembly process and excellent mechanical strength, which can meet the needs of more application scenarios and become the main focus in the field of flexible energy storage devices in the near future.[6−9]

The electrode material is the key component of a supercapacitor, which determines the specific capacity, energy and power density, and cycle stability of the supercapacitor. Molybdenum disulfide (MoS_2) is a kind of transition metal sulfide with a two-dimensional layered structure similar to graphene. It has good mechanical properties and bulk density, higher ionic conductivity, and theoretical specific capacitance than general metal oxides. It is an ultrathin flexible supercapacitor electrode material with great application potential.[10,11] Nanostructured MoS_2 has a unique crystal structure and electronic properties. As an electrode material of supercapacitor, MoS_2 has three types of charge storage mechanisms, namely, the interfacial double electric layer on the surface, the redox reaction of Mo^{4+}, and the embedded pseudocapacitance contributed by the rapid and reversible insertion of electrolyte ions between its layers. Moreover, the large layer spacing (0.615 nm) of MoS_2 will accelerate the deinsertion and insertion of electrolyte ions (H^+, K^+, NH^{4+}) between the layers, resulting in a theoretical capacity of 1200 F/g. However, MoS_2 is still restricted by some problems when it is used as electrode material for supercapacitors. First, MoS_2 has low conductivity. Second, MoS_2 is prone to stacking and agglomeration in the process of rapid ion deinsertion and

Received: March 24, 2022
Accepted: April 4, 2022
Published: April 15, 2022

insertion, which leads to the rapid decay of specific capacity and deterioration of cycle performance.[12−14]

To solve the above defects, the electrochemical performance of MoS_2 can be improved by optimizing the atomic structure and surface properties of MoS_2 and forming new MoS_2 composites with other highly conductive materials. It is one of the most convenient and effective ways to improve the electrochemical performance of composite electrodes by compounding with electrode materials that have complementary and synergistic effects on microstructure, crystal structure, electrical conductivity, and electrochemical performance. Among them, carbon nanotube (CNT) with ideal one-dimensional structure, excellent electrical conductivity, and large specific surface area is one of the more ideal carbon materials for the construction of MoS_2 composites.[15−19] The addition of CNT can inhibit the agglomeration and accumulation of MoS_2 nanosheets, expand the layer spacing of MoS_2, enhance the interlayer conductivity of MoS_2, and make the redox reaction of MO^{4+} go deeper into the interlayer of MoS_2.[20−24] Although CNT can accelerate the electron transfer efficiency of MoS_2−CNT composite electrodes, the weak interaction between them will significantly reduce the flexibility of composite electrodes and limit its development in flexible supercapacitor. Therefore, we can introduce a certain amount of nanocellulose into MoS_2−CNT composite electrodes to improve their flexibility. TEMPO-oxidized cellulose nanofiber (CNF) has abundant hydroxyl and carboxyl groups and a high aspect ratio (diameter ≈ 3.5 nm, length up to tens of microns), which can not only improve the dispersion of MoS_2 and CNT, but also form a hydrogen bond between MoS_2 and CNT so that the composite electrodes have high mechanical strength without sacrificing their electrochemical properties.[25−29] In addition, CNF can also form a good three-dimensional network structure aerogel with MoS_2 and CNT. The composite aerogels have the advantages of high porosity, high pore volume, and high specific surface area, which can further enhance the electrochemical performance of composite electrodes.[30−33]

In this Article, carboxylic single-wall carbon nanotube (SWCNT) with good conductivity was used to intercalate and compound MoS_2 nanosheets to improve their electrochemical properties, and CNF with rich surface groups and flexibility was used to improve the mechanical properties of MoS_2−SWCNT composites. First, excellent MoS_2−SWCNT/CNF aqueous suspension was prepared by virtue of the excellent dispersibility of CNF. Second, MoS_2−SWCNT/CNF hybrid hydrogel was prepared by a simple hydrogen bond cross-linking method using the principle of organic/inorganic hybrid. Finally, MoS_2−SWCNT/CNF hybrid aerogel was obtained by supercritical CO_2 drying technology, and aerogel film was obtained after compression. The aerogel film has a three-dimensional network porous structure coexisting with micropores, mesopores, and macropores, and the pore structures are interconnected. The porous structure gives more contact area between MoS_2 nanosheets and the electrolytes and provides more paths for Mo^{4+} transmission. The symmetric all-solid-state flexible supercapacitor assembled with this aerogel film showed high specific capacity (area specific capacitance of 605.32 mF cm^{-2} at the scanning speed of 2 mV s^{-1}) and excellent cycle performance (91.01% specific capacity retention rate after 10 000 cycles). It still had the high specific capacity and charge−discharge performance even at a working voltage of 1.5 V. Because of the excellent flexibility of aerogel film, the assembled flexible supercapacitor still had good working stability under different bending states. This study not only enhanced the comprehensive performance of MoS_2 but also expanded its application in the field of lightweight, flexible, and high-performance energy storage.

EXPERIMENTAL SECTION

Synthesis of a MoS_2−SWCNT Aqueous Dispersion. SWCNT powder (0.15 g, OD = 1−2 nm, length = 5−30 μm, XFNANO) was added to 150 g of 1 mg/mL MoS_2 monolayer aqueous dispersion (flake thickness = 1−2 nm, XFNANO), and the mixture was dispersed under magnetic stirring for 0.5 h and, then, ultrasonically dispersed in an ice water bath for 5 min to obtain MoS_2−SWCNT aqueous dispersion.

Synthesis of a MoS_2−SWCNT/CNF Aqueous Dispersion. Two hundred fifty grams of 0.48, 0.18, and 0.08 wt % CNF aqueous dispersion were added to the above MoS_2/SWCNT aqueous dispersion, respectively. First, they were dispersed under magnetic stirring for 1 h and, then, ultrasonically dispersed in an ice water bath for 10 min to obtain MoS_2−SWCNT/CNF aqueous dispersion with CNF: MoS_2−SWCNT dry weight ratio of 4:1, 3:2, and 2:3, respectively. CNF was prepared by the method of literature.[34]

Synthesis of a MoS_2−SWCNT/CNF Hybrid Aerogel. The MoS_2−SWCNT/CNF aqueous dispersion was placed in a sample tank and placed in the hydrochloric acid atmosphere for 6 h. Under the action of hydrogen bonding, the aqueous dispersion formed a hydrogel. The hydrogel was taken out from the sample tank and replaced with deionized water several times to make pH neutral. Then, it was replaced with anhydrous ethanol many times to make it into an alcohol gel. Finally, MoS_2−SWCNT/CNF aerogel was obtained by supercritical drying under the conditions of temperature 50 °C, pressure 12 MPa, and CO_2 flow rate 20 g/min. The aerogel was compressed into an aerogel film at 5 MPa.

Synthesis of an All-Solid-State Flexible Symmetric Supercapacitor. The PVA/H_2SO_4 gel electrolyte was obtained by fully dissolving 10 g of poly(vinyl alcohol) (PVA), 10 g of concentrated sulfuric acid (H_2SO_4), and 100 g of deionized water. The aerogel electrode was prepared by cutting the aerogel film of a certain size and bonding one side of it with aluminum foil through the conductive silver paste. The other side of the aerogel electrode was then completely immersed in the gel electrolyte for 3 h. After it was removed, it was dried naturally until the surface of the aerogel electrode was dry basically. The two groups of aerogel electrodes were pressed together under 0.5 MPa to form an all-solid-state flexible symmetric supercapacitor. The MoS_2−SWCNT/CNF aerogel film held the post of both a negative and a positive electrode and was separated by the PVA/H_2SO_4 gel electrolyte. According to the CNF: MoS_2−SWCNT dry weight ratio of 4:1, 3:2, and 2:3, the supercapacitors were marked as MoSCF1, MoSCF2, and MoSCF3, respectively.

Electrochemical Measurements. The electrochemical properties of all-solid-state flexible symmetric supercapacitors MoSCF1, MoSCF2, and MoSCF3 were tested by an electrochemical workstation (Ivium-n-Stat, Ivium Technologies B.V., Netherlands). The test mode was two-electrode mode. Cyclic voltammetry (CV) at different scanning rates and galvanostatic charge/discharge (GCD) at different current densities were tested at 0−0.8 V voltages. For the electrochemical impedance spectroscopy (EIS) test, the frequency

https://doi.org/10.1021/acsomega.2c01815
ACS Omega 2022, 7, 14390−14399

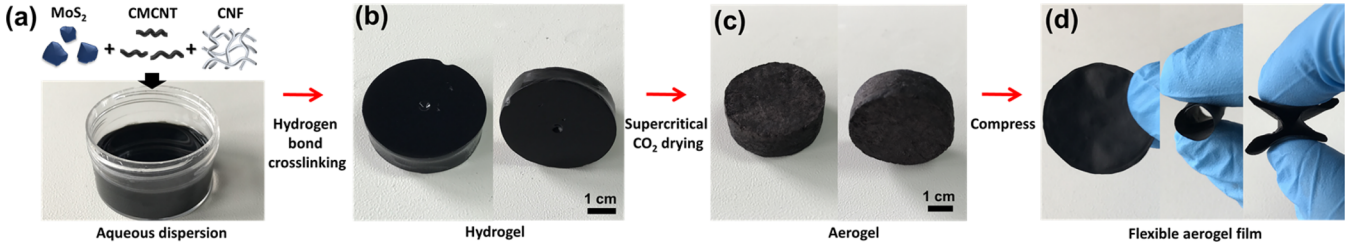

Figure 1. Schematic diagram of preparation process of MoS_2−SWCNT/CNF aerogel and aerogel film. (a) MoS_2−SWCNT/CNF aqueous dispersible solution. (b) MoS_2−SWCNT/CNF hydrogel. (c) MoS_2−SWCNT/CNF aerogel. (d) MoS_2−SWCNT/CNF flexible aerogel film.

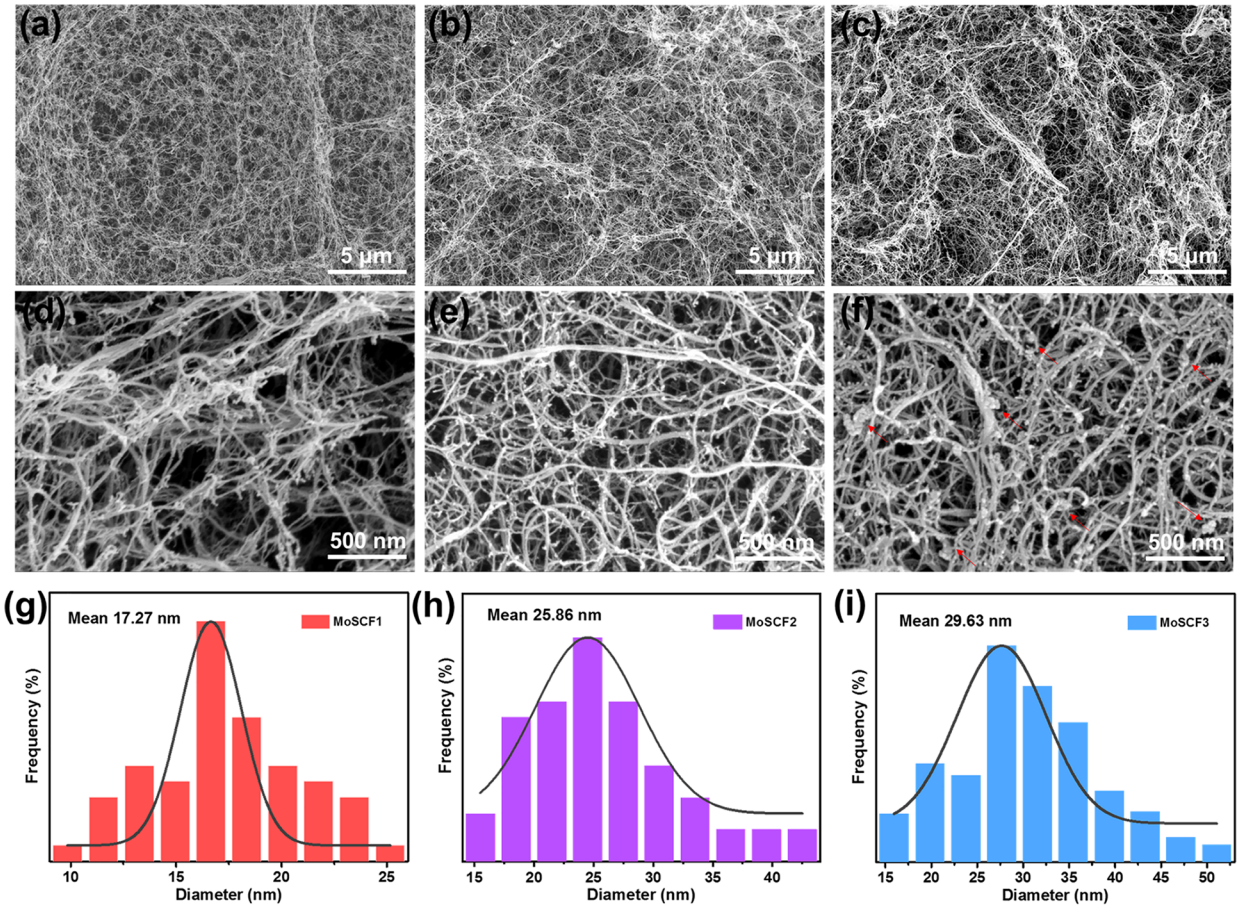

Figure 2. SEM images of (a, d) MoSCF1, (b, e) MoSCF2, and (c, f) MoSCF3 aerogels under different magnification ratios. Diameter of distributions of (g) MoSCF1, (h) MoSCF2, and (i) MoSCF3.

range was 10^{-2}−10^{5} Hz and the amplitude was 10 mV. Areal specific capacitances C_s and $C_{s'}$ calculation formula are

$$C_s = 4\left(\int I\,dU\right)/(\nu SU) \quad (1)$$

$$C_{s'} = 4(I\Delta t)/(SU) \quad (2)$$

$$C_g = 4(I\Delta t)/(mU) \quad (3)$$

where I (A), ν (V s^{-1}), S (cm^2), m (g), U (V), and Δt (s), are referred to the current, voltage scanning rate, working area of the electrode, total electrode weight, voltage window, and discharge time, respectively. Area specific energy E (mWh cm^{-2}) and area specific power P (mW cm^{-2}) could be calculated by using formulas 4 and 5.

$$E = 1/4(U^2C_{s'}/2) \quad (4)$$

$$P = E/\Delta t \quad (5)$$

Characterization Method. The morphology of aerogel was observed by scanning electron microscopy (SEM, Hitachi S-4800, Japan) and transmission electron microscopy (TEM, JEM-2100F, JEOL, Japan) with energy disperse spectroscopy (EDS, GENESIS, EDAX, USA). BET-specific surface area and BJH pore size distribution of aerogel were also measured by the N_2 adsorption instrument (ASAP2460, Micromeritics, USA). The crystal shape of aerogel was also analyzed by an X-ray diffractometer (XRD, D8 Advance). Cu K_α radiation was used (λ = 0.154 nm, 40 kV, 40 mA). The scanning range was 5−80°, and the scanning speed was 6 deg/min. The functional group structure of aerogel was also recorded by Fourier transform infrared spectrometer (FTIR, Nicolet iS10, Thermo Fisher Scientific Inc., USA). The surface chemical valence state of aerogel was also carried out by X-ray photoelectron

https://doi.org/10.1021/acsomega.2c01815
ACS Omega 2022, 7, 14390−14399

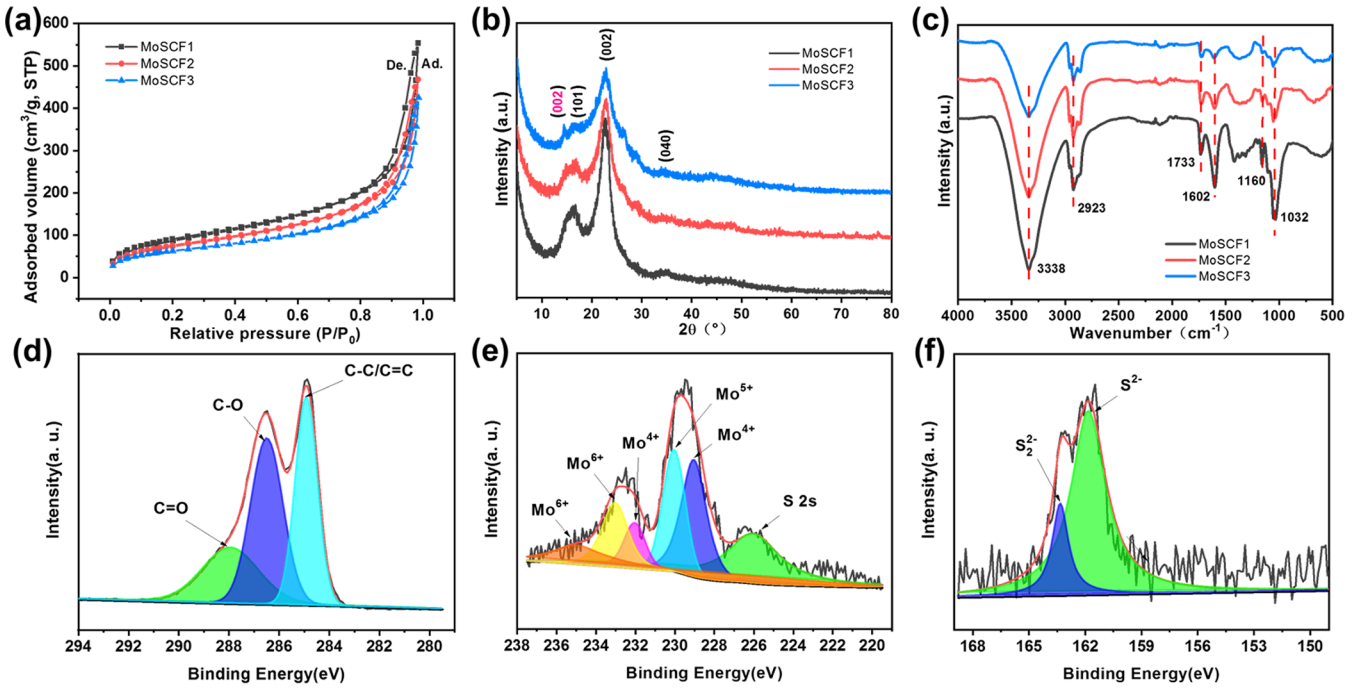

Figure 3. (a) Nitrogen adsorption/desorption isotherms, (b) XRD diagrams, and (c) FTIR spectra of MoSCF1, MoSCF2, and MoSCF3 aerogels. (d) C 1s, (e) Mo 3d, and (f) S 2p XPS spectrum of MoSCF3 aerogel.

spectroscopy (XPS, ESCALAB 250Xi, Thermo Fisher Scientific Inc., USA) with Al Ka as radiation source ($h\nu$ = 1486.6 eV, 20 mA). Tensile properties of the aerogel films were measured by a universal testing machine (MTS E43.104, US) equipped at a speed of 1 mm/min at room temperature. Conductivity was measured using a four-point probe resistivity measurement system (ST 2253, Suzhou Jingge Electronic Co., Ltd., China).

RESULTS AND DISCUSSION

The schematic diagram of the preparation process of this study is shown in Figure 1. First, the SWCNT was added to the monolayer dispersion of MoS_2, and the MoS_2 nanosheet layers were inserted with the long fiber structure of the SWCNT, and the distance between the nanosheet layers was enlarged, and the conductivity between the layers was enhanced. Subsequently, the addition of CNF can further improve the dispersion of MoS_2 and SWCNT, thus forming a good MoS_2−SWCNT/CNF aqueous dispersion (Figure 1a). Because of the abundant carboxyl groups on the surface of CNF and SWCNT, MoS_2−SWCNT/CNF aqueous dispersions will form a stable hydrogel under the action of hydrogen bonding (Figure 1b).After that, the supercritical CO_2 drying technique could be used to maximize the stability of the porous structure and obtain an aerogel with an excellent fibrous network structure (Figure 1c). Finally, the aerogel formed an aerogel film at a pressure of 5 MPa. The aerogel film had good flexibility and could be crimped and folded without rupture (Figure 1d), which was due to the good flexibility of CNF.

The microstructure characterization of different ratios of MoS_2−SWCNT/CNF aerogels was performed using an SEM, as shown in Figure 2. SEM showed that MoSCF1, MoSCF2, and MoSCF3 aerogels had interwoven fibrous porous network structures (Figure 2a−c). In the SEM images with larger magnification (Figure 2d−f), the fiber diameters of the three kinds of aerogel were statistically analyzed to obtain their frequency histogram (Figure 2g−i). According to the normal distribution fitting calculation, the diameters of MoSCF1, MoSCF2, and MoSCF3 aerogels were concentrated in 17.27, 25.86, and 29.63 nm, respectively. It was obvious that the average diameter of aerogels increased with the increase of MoS_2−SWCNT content. As the MoS_2−SWCNT content increased, the fibrous porous network structure did not change significantly, and only the fiber surface became rougher (Figure 2d−f). For MoSCF3, we could clearly see the existence of MoS_2 at the nanoscale, as shown by the red arrow in Figure 2f. It could be seen that MoS_2 had good dispersion in aerogel without obvious accumulation. In the TEM of sample MoSCF3, we could also find the same distribution, as shown by the red arrow in Figure S1a. At high magnification, MoS_2 presented a nano-flake structure (Figure S1b). TEM also showed that aerogel had interwoven fibrous network structure (Figure S1a).

To further analyze the porous structure characteristics of the aerogel, the specific surface area and pore size distribution were characterized, as shown by nitrogen adsorption/desorption isotherms (Figure 3a) and pore size distribution curves obtained by the BJH model (Figure S2a). The specific surface area of MoSCF1, MoSCF2, and MoSCF3 aerogels was 328.86, 280.23, and 229.86 $m^2\ g^{-1}$, and the pore volume was 0.83, 0.70, and 0.64 $cm^3\ g^{-1}$, respectively, indicating that all aerogels had high specific surface area and pore volume. The above aerogel also had a small pore size, and the average pore size was 9.73, 10.46, and 11.81 nm, respectively. As the MoS_2−SWCNT content increased, the specific surface area and pore volume decreased, while the average pore size increased gradually. This is also consistent with the average diameter distribution of the fibers in the aerogel of Figure 2. This indicated that the less proportion of CNF, the worse the dispersion effect of CNF on MoS_2−SWCNT, and the smaller the hydrogen bond density of the formed aerogel. Therefore, during the drying process of supercritical CO_2, the proportion

https://doi.org/10.1021/acsomega.2c01815
ACS Omega 2022, 7, 14390−14399

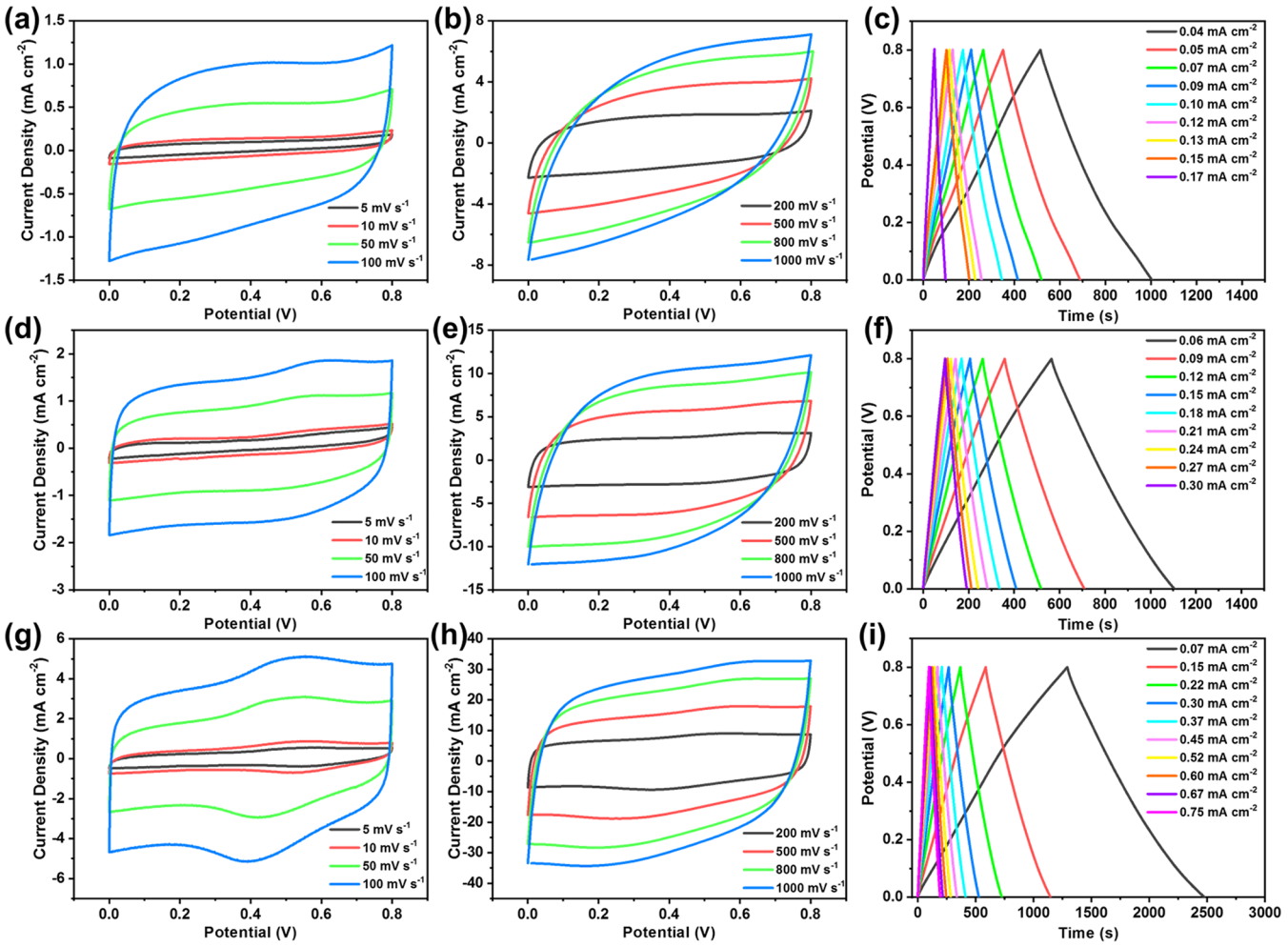

Figure 4. CV curves of (a, b) MoSCF1, (d, e) MoSCF2, and (g, h) MoSCF3 all-solid-state flexible supercapacitor electrodes at different scanning rates. GCD curves of (c) MoSCF1, (f) MoSCF2, and (i) MoSCF3 all-solid-state flexible supercapacitor electrodes at different current densities.

of aerogel internal structure collapse was more, resulting in the specific surface area and pore volume of the aerogel gradually decreasing.[35]

The crystallinity of the aerogel was analyzed, as shown in Figure 3b. The XRD spectrum of MoSCF1 mainly presented the characteristic peaks of CNF, and the peaks at 16.1°, 22.8°, and 34.5° were the characteristic peaks of (101), (002), and (040) of cellulose I. With the increase of MoS_2−SWCNT content, the characteristic peaks at (101) and (040) gradually disappeared, and the intensity of the characteristic peak at (002) also gradually weakened. MoSCF3 had a characteristic peak of MoS_2 (002) at 14.4°.[36] The FTIR spectra of aerogels showed that all the peaks at 3338 and 2923 cm^{-1} corresponded to the stretching vibration absorption peaks of −OH and C−H. The peaks at 1733 and 1602 cm^{-1} corresponded to the C═O stretching vibration absorption peak after TEMPO oxidation. The peaks at 1160 and 1032 cm^{-1} correspond to the stretching vibration absorption peaks of C−C and C−O, respectively (Figure 3c). This indicated that aerogel mainly retained the characteristic peak of CNF.[37] With the increase of MoS_2−SWCNT content, the above characteristic peaks gradually weakened. The XPS spectrum of aerogel showed characteristic peaks of O, C, Mo, and S elements (Figure S2b and S2c). Among them, C and O elements mainly came from CNF and SWCNT, and their characteristic peak signals were strong, while Mo and S elements came from MoS_2, and their characteristic peak signals were weaker. XPS peaks of MoSCF3 aerogel with the highest MoS_2−SWCNT content were processed by peak separation (Figure 3d−f), and the characteristic peaks of C 1s at 284.8, 286.5, and 288.0 eV corresponded to C−C/C═C, C−O, and C═O bonds in CNF and SWCNT, respectively.[38] After the MO 3d peak was separated, the 226.1 eV characteristic peak corresponded to MoS_2 S 2s,[39] and the characteristic peaks at 232.1 and 228.9 eV corresponded to Mo $3d_{1/2}$ and Mo $3D_{5/2}$ of Mo^{4+}, respectively.[40] The characteristic peaks at 235.1 and 233.1 eV corresponded to Mo^{6+} in a small amount of MoO_3, and the characteristic peak at 229.9 eV corresponded to MO^{5+} partially reduced by Mo^{6+} (Figure 3e).[41] The characteristic peaks of S 2p at 161.7 and 163.2 eV corresponded to S $2p_{3/2}$ of S^{2-} and S $2p_{1/2}$ of S_2^{2-}, respectively (Figure 3f).[42] Furthermore, the conductivities of MoSCF1, MoSCF2 and MoSCF3 aerogel films are 0.38, 0.79, and 1.27 S cm^{-1}, respectively, which showed good conductivity (Figure S2d).

Electrochemical performance analysis of three symmetric all-solid-state flexible supercapacitors, MoSCF1, MoSCF2, and MoSCF3, was conducted respectively, as shown in Figure 4. Figures 4a, 4d, and 4g showed the CV curves of MoSCF1, MoSCF2, and MoSCF3 at different scanning rates of 5, 10, 50, and 100 mV s^{-1}, respectively. It can be seen that the three electrodes all presented regular rectangular CV curves, and the CV curves had good symmetry, indicating that the three

https://doi.org/10.1021/acsomega.2c01815
ACS Omega 2022, 7, 14390−14399

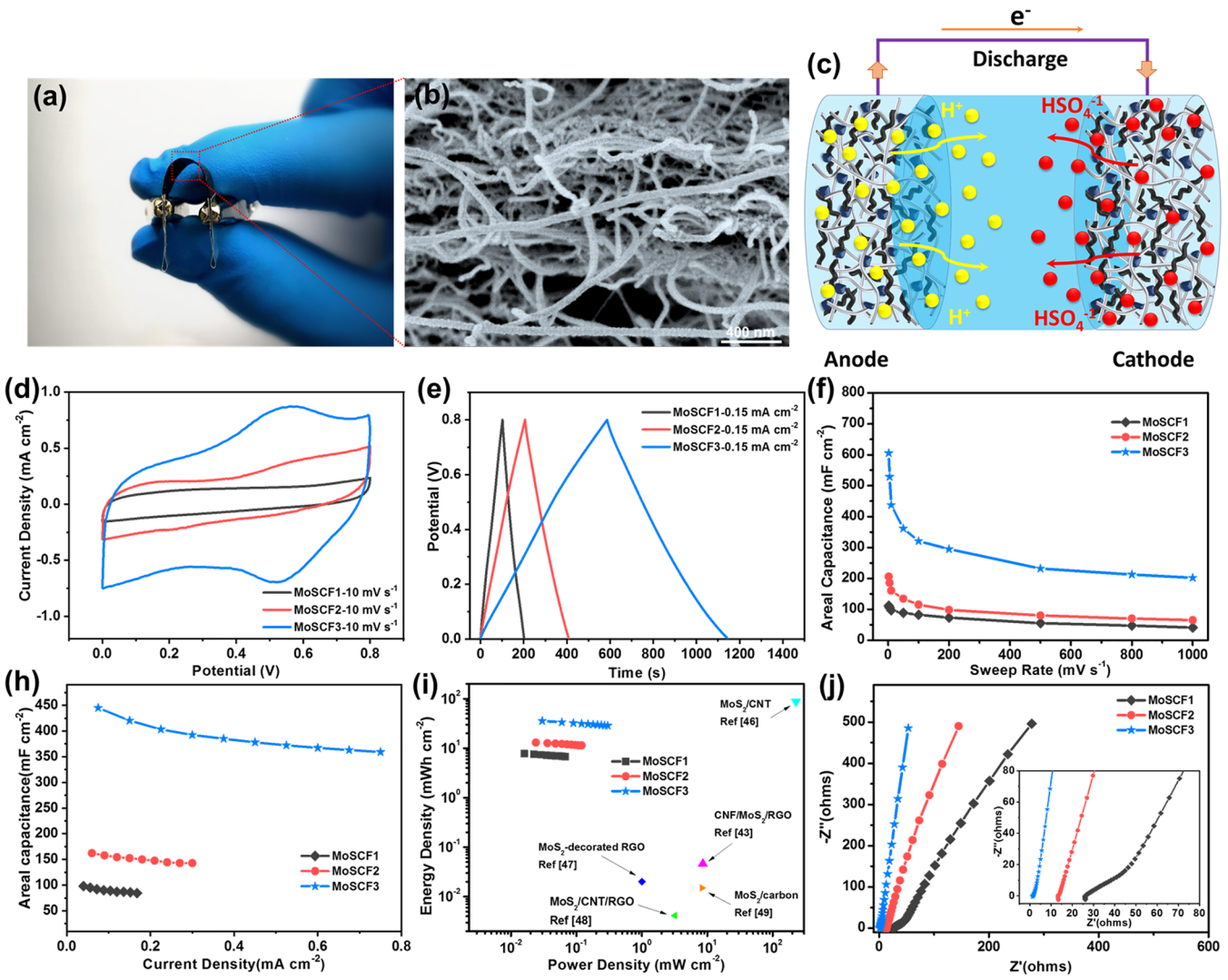

Figure 5. (a) Optical image of MoSCF3 supercapacitor device. (b) SEM image of cross section of MoSCF3 electrode. (c) Schematic diagram of ion diffusion in electrode porous network at the electrode/electrolyte interface. (d) CV curve and (e) GCD curve of MoSCF1, MoSCF2, and MoSCF3 supercapacitor electrodes at the same scanning rate and the same current density. The area specific capacitance of MoSCF1, MoSCF2, and MoSCF3 supercapacitor electrodes at (f) different scanning rates and (h) different current densities. (i) Area specific power and area specific energy of MoSCF1, MoSCF2, and MoSCF3 supercapacitors and other reported data. (j) EIS curves of MoSCF1, MoSCF2, and MoSCF3 supercapacitors.

supercapacitors all had good cycle reversibility. MoSCF1 was a typical electric double layer capacitor. With the increase of MoS_2−SWCNT content, the CV curve began to exhibit the dual characteristics of electric double layer capacitor and Faraday pseudocapacitance. Especially, MoSCF3 with the highest MoS_2−SWCNT content appeared the redox reaction peak of Mo^{4+}. Figure 4b, 4e, and 4h showed the CV curves of MoSCF1, MoSCF2, and MoSCF3 at different scanning rates of 200, 500, 800, and 1000 mV s^{-1}, respectively. It can be seen that the CV curve of MoSCF1 gradually deformed with the increase of scanning rate, especially at 1000 mV s^{-1}, the CV curve deformed obviously and became a typical shuttle shape. MoSCF2 only had a slight variation in 1000 mV s^{-1}, while MoSCF3 with the highest MoS_2−SWCNT content still maintained a good rectangular shape, indicating that with the increase of MoS_2−SWCNT content, the reversibility of cyclic voltammograms was better and the rate capability was higher. According to the formula $I = av^b$, where I and v are current density and scan rate, respectively, and a and b are fitting parameters obtained from log I versus log v plots (Figures S3). The resulting b-values of oxidation peak and reduction peak of MoSCF3 was 0.76 and 0.86. When the value of b is close to 0.5, it is a diffusion-limited Faradaic processes. When the value of b is close to 1, it is indicative of capacitive currents. The b value of MoSCF3 indicated that it was closer to capacitive in nature. Figure 4c, 4f, and 4i showed the GCD curves of MoSCF1, MoSCF2, and MoSCF3 under different current densities, respectively. It can be seen that the three electrodes all presented regular symmetrical triangular curves and had good Coulombic efficiency. In particular, MoSCF3 with the highest MoS_2−SWCNT content had a charge−discharge time close to 2500s under the current density of 0.07 mA cm^{-2}. It still maintained a good symmetrical triangular curve and the Coulombic efficiency still reached 91.9% (Figure S4).

After compression, the aerogel film still has a good porous network structure, as shown in Figure 5a and b. The perforated porous network structure could promote better ion migration and diffusion in the pores, as shown in Figure 5c. During the

https://doi.org/10.1021/acsomega.2c01815
ACS Omega 2022, 7, 14390−14399

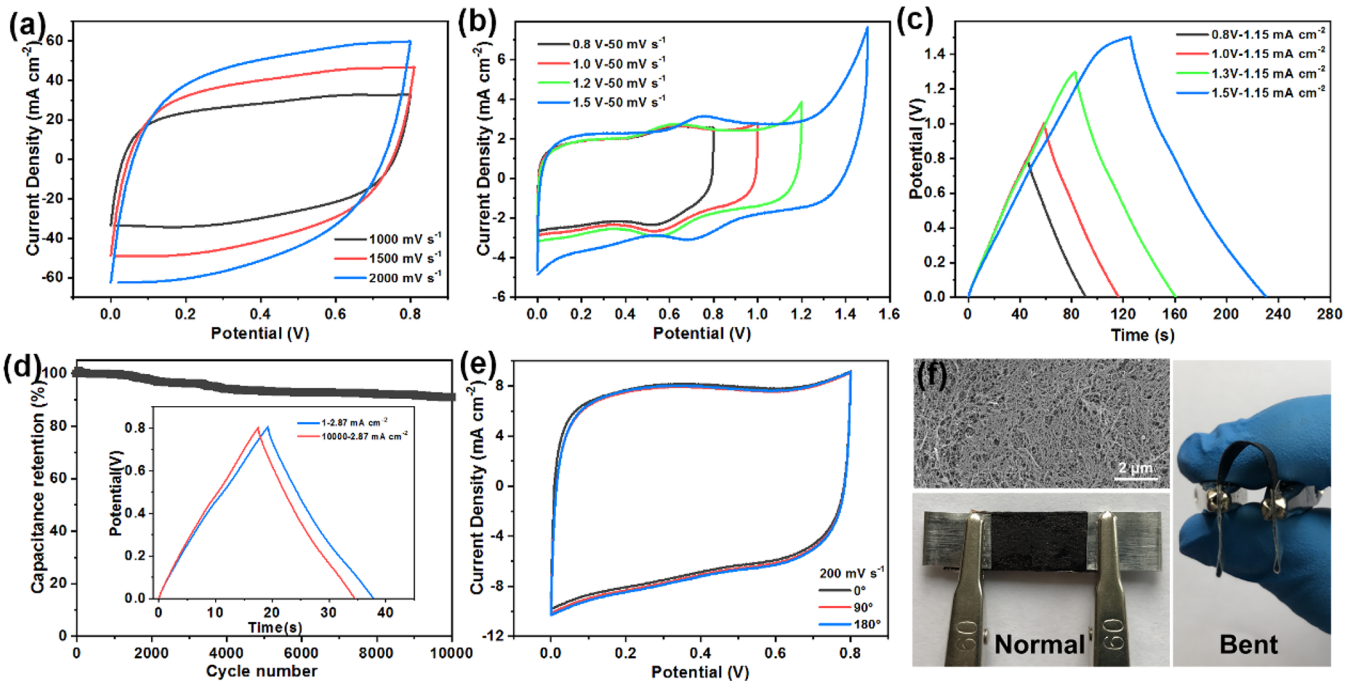

Figure 6. (a) CV curves of MoSCF3 supercapacitor electrode at high scanning rates. (b) CV curves and (c) GCD curves of MoSCF3 supercapacitor electrode under different voltage windows. (d) Cyclic stability test of MoSCF3 supercapacitor electrode. The inner figure is the GCD curve before and after 10000 charges and discharges. (e) CV curves of MoSCF3 supercapacitor electrode at different bending angles. (f) Appearance image of MoSCF3 supercapacitor device in normal and bent states. The upper left corner is the SEM image of the surface of MoSCF3 aerogel film.

process of charge transfer, H^+ ions in the electrolyte would diffuse into the porous network structure of MoS_2−SWCNT/CNF electrode. Figure 5d showed the CV curves of MoSCF1, MoSCF2, and MoSCF3 at the scanning rate of 10 mV s^{-1}. By comparison, it was found that the CV curve of MoSCF3 had obvious redox reaction peaks, and the integral area of the CV curve was the largest. Even at 1000 mV s^{-1}, the CV curve integral area of MoSCF3 was the largest (Figure S5). This indicated that the higher the MoS_2−SWCNT content, the better the electrochemical performance of the aerogel electrode. The area ratio capacity Cs calculated at different scanning rates indicated that MoSCF3 had a higher Cs, as shown in Figure 5f. At the scanning rate of 2 mV s^{-1}, the area specific capacities of MoSCF1, MoSCF2 and MoSCF3 reached 111.29, 205.61, and 605.32 mF cm^{-2}, respectively. Even at 10 mV s^{-1}, MoSCF3 still had an area specific capacity of 437.47 mF cm^{-2}. Compared with the results of CNFs/MoS_2/RGO hybrid aerogel (458.21 mF cm^{-2}),[43] MoS_2/CNT on cellulose paper (16.3 mF cm^{-2}),[44] MoS_2 on pyrolyzed cellulose paper (47.7 mF cm^{-2}),[45] MoS_2 on CNT sheets (340 mF cm^{-2}),[46] MoS_2-decorated RGO (14 mF cm^{-2}),[47] MoS_2@CNT/RGO film (29.5 mF cm^{-2}),[48] MoS_2 on carbon cloth (55.2 mF cm^{-2}),[49] and MoS_2/RGO/CNT hybrid fibers (93.2 mF cm^{-2})[50] electrodes in the literature, the area ratio of MoSCF3 was higher, indicating that, MoS_2, SWCNT, and CNF had a synergistic effect. The energy storage mechanism of the MOS_2−SWCNT/CNF electrode was that it had a dual behaviors of electric double layer capacitor and Faraday pseudocapacitance. The addition of SWCNT could not only reduce the accumulation of MoS_2, but also increas the conductivity of MoS_2, thereby providing more electron conductivity channels for the MoS_2−SWCNT composite electrode, and accelerating the overall electron transfer ability of the composite electrode. At the same time, the porous aerogel structure formed by CNF also provided more active sites for electron transport and ion diffusion, endowed more contact area between MoS_2−SWCNT and electrolyte, and provided multiple paths for Mo^{4+} transmission. Figure 5e showed the GCD curves of MoSCF1, MoSCF2, and MoSCF3 at the current density of 0.15 mA cm^{-2}. It can be seen that MoSCF3 has the longest charging and discharging time under the same current density. GCD data of MoSCF1, MoSCF2, and MoSCF3 under different current densities were calculated to obtain their area specific capacity $C_{s'}$ and gravimetric specific capacitance C_g, as shown in Figures 5h and S6. At the same current density of 0.15 mA cm^{-2}, $C_{s'}$ of MoSCF1, MoSCF2, and MoSCF3 were 86.18, 152.55, and 420.45 mF cm^{-2}, respectively. It indicated that the higher the MoS_2−SWCNT content, the larger the area specific capacity of the electrode. When the current density was 0.075 mA cm^{-2}, $C_{s'}$ of MoSCF3 achieved a maximum of 445.20 mF cm^{-2}. Even when the current density increased to 0.75 mA cm^{-2}, $C_{s'}$ still had 359.25 mF cm^{-2}, which had reached more than 80% of the maximum specific capacity, indicating that MoSCF3 had very good rate capability. The mass loadings of MoSCF1, MoSCF2, and MoSCF3 were1.30, 1.93, and 3.37 mg cm^{-2}, respectively. Thus, C_g of MoSCF1, MoSCF2, and MoSCF3 could reach 18.85 (0.015 A g^{-1}), 21.07 (0.015 A g^{-1}), and 30.34 F g^{-1} (0.01 A g^{-1}), respectively (Figure S6). According to reports, when the two-dimensional nanomaterial was used as an electrode, the disordered stacking of the two-dimensional nanoflake was the main reason for the poor charge−discharge performance and specific capacity loss.[51] SWCNT and CNF can not only reduce the accumulation of MoS_2 but also ensure the structural stability of MOS_2−SWCNT/CNF composite electrode in the charge−discharge cycle because of the

https://doi.org/10.1021/acsomega.2c01815
ACS Omega 2022, 7, 14390−14399

inherent flexibility of CNF. One possible mechanism that promoted charge storage on MOS_2−SWCNT/CNF electrodes was the integration of proton insertion/deinsertion during redox reactions (Figure 5c). During the electric double layer capacitor and Faraday pseudocapacitance process, the proton adsorption/desorption on MOS_2−SWCNT/CNF surfaces was as follows:[52,53]

$$MoS_2 + H^+ + e^- \leftrightarrow MoS{-}SH \quad (6)$$

$$(MoS_2)_{surface} + H^+ + e^- \leftrightarrow (MoS{-}H^+)_{surface} \quad (7)$$

According to GCD curves of different current densities, the corresponding area ratio power P and area ratio energy E were calculated respectively, as shown in Figure 5i. The area specific energy of MoSCF1 ranged from 7.84 to 6.74 mWh cm^{-2} at the area specific power of 0.016 to 0.0672 mW cm^{-2}. MoSCF2 had an area specific energy from 12.97 to 11.43 mWh cm^{-2} at an area specific power of 0.024 to 0.12 mW cm^{-2}. When the area specific power of MoSCF3 varied from 0.03 to 0.3 mW cm^{-2}, the area specific energy varied from 35.61 to 28.74 mWh cm^{-2}. It can be seen that MoSCF3 still had the highest area specific energy. These area specific power and area specific energy results were comparable with or higher than those of the recently reported flexible supercapacitors.[43,46−49] To further investigate the electrolyte ion transport properties of the supercapacitor, EIS tests were carried out on MoSCF1, MoSCF2, and MoSCF3, as shown in Figure 5j. The sequence of equivalent series resistance (R_s) of supercapacitor was MoSCF3 (1.32 Ω) < MoSCF2 (13.43 Ω) < MoSCF1 (26.13 Ω), which indicated that MoSCF3 had better conductivity. MoSCF3 had no obvious semicircle in the high-frequency region, indicating that its charge transfer resistance (R_{ct}) is very small. The straight line in the low-frequency region was close to 90°, indicating that MoSCF3 had faster ion transport capability and faster frequency responsiveness. Bode plots of the MoSCF1, MoSCF2, and MoSCF3 also showed that the impedance Z sharply decreased as the frequency increased and then the curve stabilized gradually (Figure S7). At the same frequency, MoSCF3 had a smaller Z value than MoSCF1 and MoSCF2.

To further explore the upper limit of electrochemical performance of MoSCF3, the CV performance test was conducted at a higher scanning rate, as shown in Figure 6a. It can be seen that MoSCF3 still had a good rectangular curve at 1500 mV s^{-1}. Even at 2000 mV s^{-1}, the CV curve was only slightly deformed. This indicated that MoSCF3 had very strong charge transfer ability and rate capability. In addition, we also conducted CV and GCD performance experiments on MoSCF3 in a higher voltage window to test its extreme electrochemical capacity, as shown in Figure 6b and 6c. It can be seen that with the increase of voltage, the integral area, and area specific capacity of the CV curve both increased (Figure S8), and the redox peak also moved to the high voltage direction, and the charge and discharge time of the GCD curve also increased gradually. The CV curve remained a good rectangular shape at 1.0 and 1.2 V, while the GCD curve maintained a good symmetrical triangular shape at 1.0 and 1.3 V. When the voltage increased to 1.5 V, the CV and GCD curves appeared slight deformation. This was because the aqueous acidic electrolyte began to hydrolyze under the high voltage window, resulting in the reduction of electrochemical stability. The above results indicated that MoSCF3 had very high voltage−resistance, and could work at a higher voltage window. To investigate the cycle stability of MoSCF3, 10 000 GCD cycles were tested at the current density of 2.87 mA cm^{-2}, as shown in Figure 6d. After 10 000 cycles, the specific capacity can maintain 91.01% of its original value, indicating excellent cyclic stability of MoSCF3. From the outside, MoSCF3 had not changed. After 10 000 cycles, the results of SEM showed that the microstructure of MoSCF3 had no obvious change (Figure S9a), and it was still a dense fibrous network structure. The XRD diffraction peak of MoSCF3 in Figure S9b also had no obvious change compared with Figure 3b. These results indicated that MoSCF3 had good cycle stability. MoSCF3 had a higher voltage window and excellent charge−discharge cycle stability. First, MoSCF3 had smaller internal resistance and higher conductivity, which was conducive to the electron diffusion and transfer, and avoided the capacity loss caused by large resistance of electron transmission due to poor electrode conductivity. Second, the porous aerogel structure with a high specific surface and high porosity provided good support for the composite electrode and provided more extension space for the small deformation caused by electrolyte ion deinsertion and insertion. Finally, in order to investigate the flexibility of MoSCF3, the CV test of flexible supercapacitor under different bending angles was carried out at a 200 mV s^{-1} scanning rate, as shown in Figure 6e. CV curves were almost unaffected by the bending angles, and MoSCF3 exhibited excellent flexible stability, which was benefited from the good mechanical flexibility of CNF itself. The MoSCF3 had a tensile strength of 20.49 MPa at a strain of 4.05% (Figure S10), which showed good mechanical property. Moreover, even if the aerogel was compressed into aerogel film under high pressure, the microscopic surface of the aerogel film still presented a porous fibrous network structure (Figure 6f). The interlaced network structure made the aerogel film have the higher specific surface area and pore volume, which is beneficial to the enhancement of electrochemical performance. At the same time, it also gave the composite electrode good flexibility, which had potential applications in flexible devices and could provide energy for wearable devices, such as watches and wristbands.

CONCLUSIONS

In this Article, a high specific surface area, flexible and self-supporting MoS_2−SWCNT/CNF aerogel film electrode was prepared by nanohybrid method and supercritical CO_2 drying technology and then assembled into a all-solid-state flexible symmetric supercapacitor. The aerogel membrane electrode had a three-dimensional fibrous porous network structure with a maximum specific surface area of 328.86 m^2 g^{-1}, a pore volume of 0.83 cm^3 g^{-1}, and a small pore size (∼10 nm). The intercalation of SWCNT inhibited the accumulation of MoS_2 nanosheets and enhanced the conductivity of the composite electrode. The dispersion of CNF further improved the structural uniformity of MoS_2 and SWCNT and endowed the composite electrode with excellent flexibility. The assembled all-solid-state flexible symmetric supercapacitor had excellent electrochemical performance, the CV curves were rectangular, and the GCD curves also had a symmetrical triangular shape. With the increase of MoS_2−SWCNT content, the specific capacity and specific energy of the supercapacitor electrode both increased. MoSCF3 with the highest MoS_2−SWCNT content had a specific capacity of 605.32 mF cm^{-2} at 2 mV s^{-1} and 30.34 F g^{-1} at 0.01 A g^{-1}. When the area specific power was 0.03 mW cm^{-2}, the area specific energy of MoSCF3

https://doi.org/10.1021/acsomega.2c01815
ACS Omega 2022, 7, 14390−14399

reached 35.61 mWh cm^{-2}. The capacity retention rate of MoSCF3 reached 91.01% after 10 000 cycles of charge and discharge. The electrochemical properties of MoSCF3 were not affected at different bending angles, showing good flexibility. In addition, the extreme voltage window of the MoSCF3 supercapacitor can reach 1.5 V, which further indicated that MoS_2−SWCNT/CNF supercapacitor had an excellent electrochemical performance. This study provided a new research idea for the application of two-dimensional materials in flexible devices.

■ ASSOCIATED CONTENT

Supporting Information

The Supporting Information is available free of charge at https://pubs.acs.org/doi/10.1021/acsomega.2c01815.

TEM, Coulombic efficiency and C_s of MoSCF3, pore size distribution, XPS, conductivities, CV curves, C_g, and bode plots of three samples, graphs of log I versus log ν for MoSCF3, and SEM and XRD of MoSCF3 after 10 000 cycles (PDF)

■ AUTHOR INFORMATION

Corresponding Author

Shaoyi Lyu − *Research Institute of Wood Industry, Chinese Academy of Forestry, Beijing 100091, China; Co-Innovation Center of Efficient Processing and Utilization of Forest Resources, Nanjing Forestry University, Nanjing 210037, China;* orcid.org/0000-0002-0299-2504; Email: lvsy@caf.ac.cn

Authors

Huanjun Chang − *Research Institute of Wood Industry, Chinese Academy of Forestry, Beijing 100091, China*

Longfei Zhang − *Research Institute of Wood Industry, Chinese Academy of Forestry, Beijing 100091, China; Co-Innovation Center of Efficient Processing and Utilization of Forest Resources, Nanjing Forestry University, Nanjing 210037, China*

Siqun Wang − *Center for Renewable Carbon, University of Tennessee, Knoxville, Tennessee 37996, United States;* orcid.org/0000-0002-5666-9390

Complete contact information is available at: https://pubs.acs.org/10.1021/acsomega.2c01815

Notes

The authors declare no competing financial interest.

■ ACKNOWLEDGMENTS

The authors acknowledge the Special Fund for Forest Scientific Research in the Public Welfare (No. 201504603).

■ REFERENCES

(1) He, W.; Fu, X.; Zhang, D.; Zhang, Q.; Zhuo, K.; Yuan, Z.; Ma, R. Recent progress of flexible/wearable self-charging power units based on triboelectric nanogenerators. *Nano Energy* **2021**, *84*, 105880.

(2) Liu, Y.; Pharr, M.; Salvatore, G. A. Lab-on-skin: a review of flexible and stretchable electronics for wearable health monitoring. *ACS Nano* **2017**, *11* (10), 9614−9635.

(3) Wang, X.; Lu, X.; Liu, B.; Chen, D.; Tong, Y.; Shen, G. Flexible energy-storage devices: design consideration and recent progress. *Adv. Mater.* **2014**, *26* (28), 4763−4782.

(4) Yousaf, M.; Shi, H. T. H.; Wang, Y.; Chen, Y.; Ma, Z.; Cao, A.; Naguib, H. E.; Han, R. P. Novel pliable electrodes for flexible electrochemical energy storage devices: recent progress and challenges. *Adv. Energy Mater.* **2016**, *6* (17), 1600490.

(5) Wang, D.; Han, C.; Mo, F.; Yang, Q.; Zhao, Y.; Li, Q.; Liang, G.; Dong, B.; Zhi, C. Energy density issues of flexible energy storage devices. *Energy Storage Mater.* **2020**, *28*, 264−292.

(6) Yang, Y. A mini-review: emerging all-solid-state energy storage electrode materials for flexible devices. *Nanoscale* **2020**, *12* (6), 3560−3573.

(7) Lv, T.; Liu, M.; Zhu, D.; Gan, L.; Chen, T. Nanocarbon-based materials for flexible all-solid-state supercapacitors. *Adv. Mater.* **2018**, *30* (17), 1705489.

(8) Yang, P.; Mai, W. Flexible solid-state electrochemical supercapacitors. *Nano Energy* **2014**, *8*, 274−290.

(9) Du, X.; Zhang, Z.; Liu, W.; Deng, Y. Nanocellulose-based conductive materials and their emerging applications in energy devices-A review. *Nano Energy* **2017**, *35*, 299−320.

(10) Bello, I. T.; Oladipo, A. O.; Adedokun, O.; Dhlamini, S. M. Recent advances on the preparation and electrochemical analysis of MoS_2-based materials for supercapacitor applications: A mini-review. *Mater. Today Commun.* **2020**, *25*, 101664.

(11) Joseph, N.; Shafi, P. M.; Bose, A. C. Recent advances in 2D-MoS_2 and its composite nanostructures for supercapacitor electrode application. *Energy Fuel.* **2020**, *34* (6), 6558−6597.

(12) Theerthagiri, J.; Senthil, R.A.; Senthilkumar, B.; Reddy Polu, A.; Madhavan, J.; Ashokkumar, M. Recent advances in MoS_2 nanostructured materials for energy and environmental applications-a review. *J. Solid State Chem.* **2017**, *252*, 43−71.

(13) Venkata Subbaiah, Y.; Saji, K.; Tiwari, A. Atomically thin MoS_2: A versatile nongraphene 2D material. *Adv. Funct. Mater.* **2016**, *26* (13), 2046−2069.

(14) Gupta, H.; Chakrabarti, S.; Mothkuri, S.; Padya, B.; Rao, T.; Jain, P. High performance supercapacitor based on 2D-MoS_2 nanostructures. *Mater. Today: Proc.* **2020**, *26*, 20−24.

(15) Sun, P.; Wang, R.; Wang, Q.; Wang, H.; Wang, X. Uniform MoS_2 nanolayer with sulfur vacancy on carbon nanotube networks as binder-free electrodes for asymmetrical supercapacitor. *Appl. Surf. Sci.* **2019**, *475*, 793−802.

(16) Chen, X.; Ding, J.; Jiang, J.; Zhuang, G.; Zhang, Z.; Yang, P. Preparation of a MoS_2/carbon nanotube composite as an electrode material for high-performance supercapacitors. *RSC Adv.* **2018**, *8* (52), 29488−29494.

(17) Yang, X.; Zhao, L.; Lian, J. Arrays of hierarchical nickel sulfides/MoS_2 nanosheets supported on carbon nanotubes backbone as advanced anode materials for asymmetric supercapacitor. *J. Power Sources* **2017**, *343*, 373−382.

(18) Wang, T.; Chen, S.; Pang, H.; Xue, H.; Yu, Y. MoS_2-based nanocomposites for electrochemical energy storage. *Adv. Sci.* **2017**, *4* (2), 1600289.

(19) Lee, C.; Ozden, S.; Tewari, C. S.; Park, O. K.; Vajtai, R.; Chatterjee, K.; Ajayan, P. M. MoS_2-Carbon Nanotube Porous 3 D Network for Enhanced Oxygen Reduction Reaction. *ChemSusChem* **2018**, *11* (17), 2960−2966.

(20) Radhakrishnan, S.; Ka, S. R.; Kumar, S. R.; Johari, P.; Rout, C. S. Energy storage performance of 2D MoS_2 and carbon nanotube heterojunctions in symmetric and asymmetric configuration. *Nanotechnology* **2021**, *32* (15), 155403.

(21) Long, J.; Hu, A.; Shu, C.; Wang, S.; Li, J.; Liang, R. Three-Dimensional Flower-Like MoS_2@ Carbon Nanotube Composites with Interconnected Porous Networks and High Catalytic Activity as Cathode for Lithium-Oxygen Batteries. *ChemElectroChem.* **2018**, *5* (19), 2816−2824.

(22) Zhou, H.; Zhang, R.; Song, S.; Xiao, C.; Gao, G.; Ding, S. Dopamine-assisted synthesis of MoS_2 nanosheets on carbon nanotube for improved lithium and sodium storage properties. *ACS Appl. Mater. Interfaces* **2018**, *1* (9), 5112−5118.

(23) Li, J.; Hou, Y.; Gao, X.; Guan, D.; Xie, Y.; Chen, J.; Yuan, C. A three-dimensionally interconnected carbon nanotube/layered MoS_2 nanohybrid network for lithium ion battery anode with superior rate capacity and long-cycle-life. *Nano Energy* **2015**, *16*, 10−18.

(24) Zhu, K.; Li, Q.; Ren, H.; Sun, Y.; Li, C.; Lv, R.; Fan, S.; Yang, J.; Guo, Y.; Liu, K. Few-Layer MoS_2 Nanosheet/Carbon Nanotube Composite Films for Long-Lifetime Lithium Storage and Hydrogen Generation. *ACS Appl. Nano Mater.* **2021**, *4* (5), 4754−4762.
(25) Li, Y.; Zhu, H.; Shen, F.; Wan, J.; Lacey, S.; Fang, Z.; Dai, H.; Hu, L. Nanocellulose as green dispersant for two-dimensional energy materials. *Nano energy* **2015**, *13*, 346−354.
(26) Wu, T.; Song, Y.; Shi, Z.; Liu, D.; Chen, S.; Xiong, C.; Yang, Q. High-performance nanogenerators based on flexible cellulose nanofibril/MoS_2 nanosheet composite piezoelectric films for energy harvesting. *Nano Energy* **2021**, *80*, 105541.
(27) Chen, S.; Li, J.; Song, Y.; Yang, Q.; Shi, Z.; Xiong, C. Flexible and environment-friendly regenerated cellulose/MoS_2 nanosheet nanogenerators with high piezoelectricity and output performance. *Cellulose* **2021**, *28*, 6513−6522.
(28) Xu, M.; Wu, T.; Song, Y.; Jiang, M.; Shi, Z.; Xiong, C.; Yang, Q. Achieving high-performance energy harvesting and self-powered sensing in a flexible cellulose nanofibril/MoS_2/$BaTiO_3$ composite piezoelectric nanogenerator. *J. Mater. Chem. C* **2021**, *9* (43), 15552−15565.
(29) Ferreira-Neto, E. P.; Ullah, S.; da Silva, T. C.; Domeneguetti, R. R.; Perissinotto, A. P.; de Vicente, F. S.; Rodrigues-Filho, U. P.; Ribeiro, S. J. Bacterial nanocellulose/MoS_2 hybrid aerogels as bifunctional adsorbent/photocatalyst membranes for in-flow water decontamination. *ACS Appl. Nano Mater.* **2020**, *12* (37), 41627−41643.
(30) Du, X.; Zhang, Z.; Liu, W.; Deng, Y. Nanocellulose-based conductive materials and their emerging applications in energy devices-A review. *Nano Energy* **2017**, *35*, 299−320.
(31) Guo, R.; Zhang, L.; Lu, Y.; Zhang, X.; Yang, D. Research progress of nanocellulose for electrochemical energy storage: A review. *J. Energy Chem.* **2020**, *51*, 342−361.
(32) Lavoine, N.; Bergström, L. Nanocellulose-based foams and aerogels: Processing, properties, and applications. *J. Mater. Chem. A* **2017**, *5* (31), 16105−16117.
(33) Chen, Y.; Zhang, L.; Yang, Y.; Pang, B.; Xu, W.; Duan, G.; Jiang, S.; Zhang, K. Recent progress on nanocellulose aerogels: preparation, modification, composite fabrication, applications. *Adv. Mater.* **2021**, *33* (11), 2005569.
(34) Saito, T.; Isogai, A. TEMPO-mediated oxidation of native cellulose. The effect of oxidation conditions on chemical and crystal structures of the water-insoluble fractions. *Biomacromolecules* **2004**, *5* (5), 1983−1989.
(35) Zu, G.; Shen, J.; Zou, L.; Wang, F.; Wang, X.; Zhang, Y.; Yao, X. Nanocellulose-derived highly porous carbon aerogels for supercapacitors. *Carbon* **2016**, *99*, 203−211.
(36) Lai, F.; Miao, Y.-E.; Huang, Y.; Zhang, Y.; Liu, T. Nitrogen-doped carbon nanofiber/molybdenum disulfide nanocomposites derived from bacterial cellulose for high-efficiency electrocatalytic hydrogen evolution reaction. *ACS Appl. Mater. Interfaces* **2016**, *8* (6), 3558−3566.
(37) Onyianta, A. J.; Dorris, M.; Williams, R. L. Aqueous morpholine pre-treatment in cellulose nanofibril (CNF) production: comparison with carboxymethylation and TEMPO oxidisation pre-treatment methods. *Cellulose* **2018**, *25* (2), 1047−1064.
(38) Guan, X.; Zhao, L.; Zhang, P.; Liu, J.; Song, X.; Gao, L. Electrode material of core-shell hybrid MoS_2@ C/CNTs with carbon intercalated few-layer MoS_2 nanosheets. *Mater. Today Energy* **2020**, *16*, 100379.
(39) Zhao, Z.-H.; Hu, X.-D.; Wang, H.; Ye, M.-Y.; Sang, Z.-Y.; Ji, H.-M.; Li, X.-L.; Dai, Y. Superelastic 3D few-layer MoS_2/carbon framework heterogeneous electrodes for highly reversible sodium-ion batteries. *Nano Energy* **2018**, *48*, 526−535.
(40) Lai, F.; Miao, Y.-E.; Huang, Y.; Zhang, Y.; Liu, T. Nitrogen-doped carbon nanofiber/molybdenum disulfide nanocomposites derived from bacterial cellulose for high-efficiency electrocatalytic hydrogen evolution reaction. *ACS Appl. Mater. Interfaces* **2016**, *8* (6), 3558−3566.
(41) Cao, S.; Shi, L.; Miao, M.; Fang, J.; Zhao, H.; Feng, X. Solution-processed flexible paper-electrode for lithium-ion batteries based on MoS_2 nanosheets exfoliated with cellulose nanofibrils. *Electrochim. Acta* **2019**, *298*, 22−30.
(42) Liu, X.; Xu, H.; Ji, H.; Zhang, K.; Wang, D. Featuring surface sodium storage properties of confined MoS_2/bacterial cellulose-derived carbon nanofibers anode. *Appl. Surf. Sci.* **2020**, *530*, 147261.
(43) Lv, Y.; Li, L.; Zhou, Y.; Yu, M.; Wang, J.; Liu, J.; Zhou, J.; Fan, Z.; Shao, Z. A cellulose-based hybrid 2D material aerogel for a flexible all-solid-state supercapacitor with high specific capacitance. *RSC Adv.* **2017**, *7* (69), 43512−43520.
(44) Liu, A.; Lv, H.; Liu, H.; Li, Q.; Zhao, H. Two dimensional MoS_2/CNT hybrid ink for paper-based capacitive energy storage. *J. Mater. Sci.-Mater. El.* **2017**, *28* (12), 8452−8459.
(45) Islam, N.; Wang, S.; Warzywoda, J.; Fan, Z. Fast supercapacitors based on vertically oriented MoS_2 nanosheets on plasma pyrolyzed cellulose filter paper. *J. Power Sources* **2018**, *400*, 277−283.
(46) Tiwari, P.; Janas, D.; Chandra, R. Self-standing MoS_2/CNT and MnO_2/CNT one dimensional core shell heterostructures for asymmetric supercapacitor application. *Carbon* **2021**, *177*, 291−303.
(47) Clerici, F.; Fontana, M.; Bianco, S.; Serrapede, M.; Perrucci, F.; Ferrero, S.; Tresso, E.; Lamberti, A. In situ MoS_2 decoration of laser-induced graphene as flexible supercapacitor electrodes. *ACS Appl. Mater. Interfaces* **2016**, *8* (16), 10459−10465.
(48) Wang, S.; Zhu, J.; Shao, Y.; Li, W.; Wu, Y.; Zhang, L.; Hao, X. Three-dimensional MoS_2@ CNT/RGO network composites for high-performance flexible supercapacitors. *Chem. Eur. J.* **2017**, *23* (14), 3438−3446.
(49) Jiang, Z.; Zhai, S.; Huang, M.; Songsiriritthigul, P.; Aung, S. H.; Oo, T. Z.; Luo, M.; Chen, F. 3D carbon nanocones/metallic MoS_2 nanosheet electrodes towards flexible supercapacitors for wearable electronics. *Energy* **2021**, *227*, 120419.
(50) Jian, X.; Li, H.; Li, H.; Li, Y.; Shang, Y. Flexible and freestanding MoS_2/rGO/CNT hybrid fibers for high-capacity all-solid supercapacitors. *Carbon* **2021**, *172*, 132−137.
(51) Han, Y.; Ge, Y.; Chao, Y.; Wang, C.; Wallace, G. G. Recent progress in 2D materials for flexible supercapacitors. *J. Energy Chem.* **2018**, *27* (1), 57−72.
(52) Soon, J. M.; Loh, K. P. Electrochemical Double-Layer Capacitance of MoS_2 Nanowall Films. *Electrochem. Solid-State Lett.* **2007**, *10*, A250.
(53) Zhao, C.; Zhou, Y.; Ge, Z.; Zhao, C.; Qian, X. Facile construction of MoS_2/RCF electrode for high-performance supercapacitor. *Carbon* **2018**, *127*, 699−706.

https://doi.org/10.1021/acsomega.2c01815
ACS Omega 2022, 7, 14390−14399